



OPEN ACCESS

EDITED BY

Cristina Falcinelli,
G. d'Annunzio University of Chieti and Pescara,
Italy

REVIEWED BY

Michele Marino,
University of Rome Tor Vergata, Italy
Monika Colombo,
Aarhus University, Denmark

*CORRESPONDENCE

Simona Celi,
✉ s.celi@ftgm.it

RECEIVED 30 April 2025

ACCEPTED 16 June 2025

PUBLISHED 03 July 2025

CITATION

Mazzoli M, Gasparotti E, Vignali E, Haxhiademi D and Celi S (2025) Impact of aortic morphology on VA-ECMO performance: a combined statistical shape modeling and CFD approach. *Front. Bioeng. Biotechnol.* 13:1620897. doi: 10.3389/fbioe.2025.1620897

COPYRIGHT

© 2025 Mazzoli, Gasparotti, Vignali, Haxhiademi and Celi. This is an open-access article distributed under the terms of the [Creative Commons Attribution License \(CC BY\)](https://creativecommons.org/licenses/by/4.0/). The use, distribution or reproduction in other forums is permitted, provided the original author(s) and the copyright owner(s) are credited and that the original publication in this journal is cited, in accordance with accepted academic practice. No use, distribution or reproduction is permitted which does not comply with these terms.

Impact of aortic morphology on VA-ECMO performance: a combined statistical shape modeling and CFD approach

Marilena Mazzoli^{1,2}, Emanuele Gasparotti¹, Emanuele Vignali¹, Dorela Haxhiademi³ and Simona Celi^{1*}

¹BioCardioLab, Bioengineering Unit, Fondazione Monasterio, Massa, Italy, ²Department of Information Engineering, University of Pisa, Pisa, Italy, ³Anesthesia and Intensive Care Unit, Fondazione Monasterio, Massa, Italy

Introduction: The veno-arterial extracorporeal membrane oxygenation (VA ECMO) system is a temporary support procedure to provide oxygenated blood in patients with cardiac or respiratory failure. Despite being widely used in clinical reality, the VA ECMO has some well-known flaws, like the formation of a 'watershed zone' as a consequence of the mixing of native blood from the left ventricle and retrograde oxygenated blood from the ECMO pump. A deeper knowledge of the watershed zone behavior could contribute to better defining the oxygenation balancing for the patient.

Methods: From this concept, this study proposes a numerical approach combined with Statistical Shape Modeling (SSM) to evaluate the effect of aortic morphology variations on the different conditions of VA ECMO support. In particular, a new SSM approach was adopted to define 48 synthetic aortic morphologies starting from patient-specific computed tomography datasets. After assessing the morphological differences, the first 10 modes were selected to generate volumetric meshes for a Computational Fluid Dynamics (CFD) analysis. A total of 20 cases were simulated in the healthy conditions, while four cases were simulated with a 70% reduction of cardiac output and three different levels of ECMO support (0, 4, and 6 L/min).

Results: From the simulated results, it was possible to assess the behavior of the watershed zone as a function of aortic morphological parameters and ECMO level.

Discussion: The results confirmed the significant effect of ECMO level on the position and distribution of the zone.

KEYWORDS

VA ECMO, computational fluid dynamics, statistical shape model, aorta, watershed zone

1 Introduction

Cardiogenic shock (CS) is a pathological condition most commonly caused by myocardial infarction, leading to a significant reduction in cardiac output (CO) due to myocardial cell death (Vrints et al., 2024). As CO decreases, the left ventricle (LV) becomes unable to supply sufficient oxygenated blood to the systemic circulation, resulting in life-threatening consequences if not promptly managed. Several mechanical support systems exist to

temporarily maintain circulation and oxygenation in patients with CS (Basir et al., 2023). Among these, veno-arterial extracorporeal membrane oxygenation (VA ECMO) is a widely adopted technique (Banfi et al., 2016). VA ECMO operates by draining venous blood through a first drainage cannula, passing it through an oxygenator with a rotary pump, and returning the oxygenated blood to the arterial circulation via a second return cannula. This process provides systemic oxygenation and supports LV function. Various cannulation strategies exist for the arterial return (Pavlushkov et al., 2017). A commonly adopted approach foresees an iliac artery percutaneous cannulation (Napp et al., 2016). In this configuration, ECMO flow is retrograde relative to native LV flow.

The VA ECMO appears to be a very successful procedure on the basis of its widespread use for the management of CS cases. Nevertheless, some pitfalls and flaws are well known to physicians. The process of VA ECMO management requires a significant level of caution and clinical experience. This aspect is underlined by the fact that, for example, there are no universally standardized protocols for VA ECMO weaning, and every individual center follows its own protocols (Tsiouris et al., 2023). One critical consideration is the increased afterload on the LV due to ECMO flow, which can exacerbate myocardial strain (Singh et al., 2020). Additional complications, including ischemia and thromboembolic events affecting the intestines, kidneys, and brain, are also reported, though their exact mechanisms remain not fully understood (Shen et al., 2022). A phenomenon frequently observed in clinical practice is the formation of a mixing region, known as the watershed zone, between the blood ejected by the LV and the blood delivered by the ECMO pump (Prisco et al., 2022). This watershed zone arises due to the retrograde nature of VA ECMO flow when peripheral cannulation is used. The behavior of this mixing zone is strongly linked to differential hypoxemia, a complication of VA ECMO in which upper and lower body regions receive blood with differing oxygenation levels (Rozenchwajg et al., 2023). Furthermore, the complex formation of this region is believed to contribute to some of the above-cited less well-understood complications associated with VA ECMO. Based on this, an enhanced knowledge of the watershed zone behavior would be pivotal for optimizing the balance between the native and newly ECMO-driven oxygenation.

Investigating these aspects of VA ECMO remains challenging due to the intricate hemodynamic interactions involved. Both benchtop experiments (Schenk et al., 2015) and computational models (Cui et al., 2023) have been employed to study ECMO-related hemodynamics. Computational Fluid Dynamics (CFD) simulations have been extensively used in this field (Gramigna et al., 2024). Some studies have investigated the effect of ECMO support on arterial perfusion (Ahmed et al., 2022) and on the afterload increase (Vignali et al., 2023); while others have analyzed local fluid dynamics at the cannulation site (Parker et al., 2024). Additionally, prior numerical investigations have explored the watershed zone's position and its variability at different ECMO flow rates (Rao et al., 2018). The morphology of the aorta is believed to play a key role in influencing the behavior of the watershed region, as highlighted in some previous publications (Khamooshi et al., 2024; Khodaei et al., 2022). Nevertheless, this statement is still to be proved, as tests on a wider number of cases are still lacking. In general, the state of the art most of the time

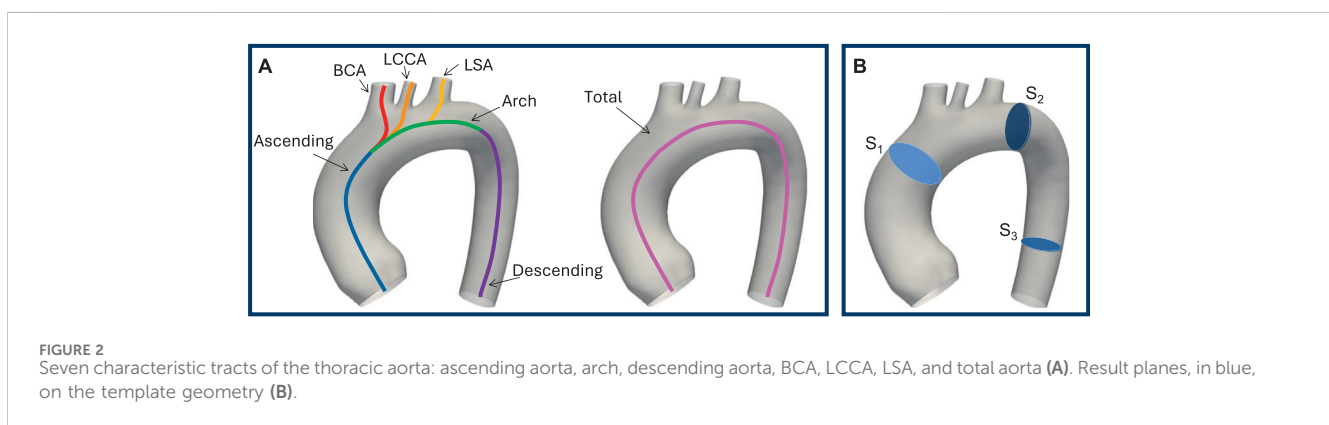
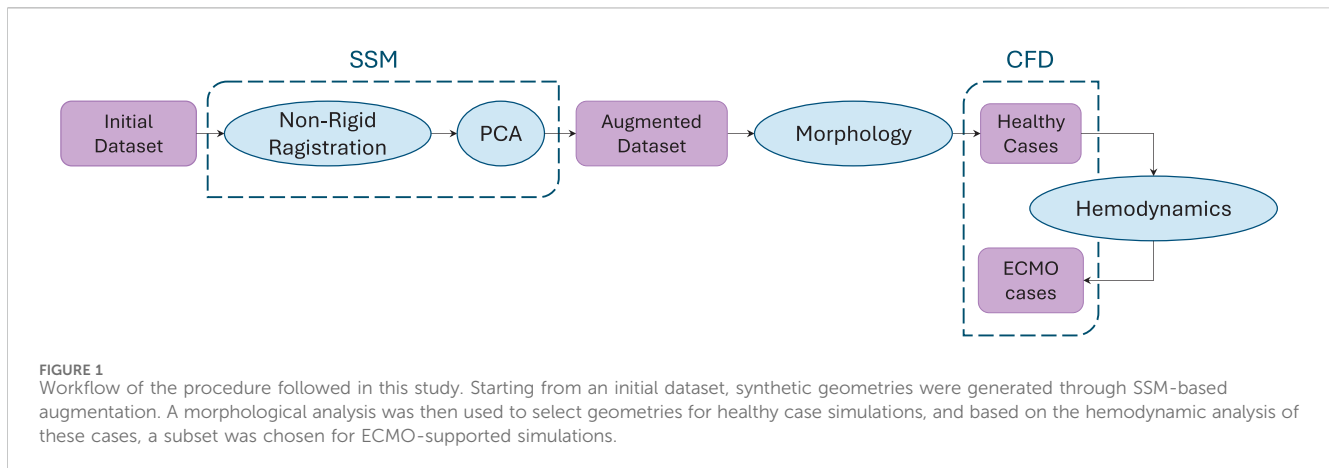
reports single case studies (Du et al., 2022) or analyses performed on idealized aortic geometries (Malinowski et al., 2023). It is well established that the morphology of the thoracic aorta exhibits considerable anatomical variability, both in the main branch and in the supra-aortic vessels (Xiong et al., 2020), which may play a key role in ECMO-induced hemodynamic changes. In this research context, Statistical Shape Modeling (SSM) is emerging as a powerful tool for conducting population-based studies (Cosentino et al., 2020; Aljassam et al., 2024). SSM enables the extraction of key morphological features that characterize a population through two main steps: non-rigid registration of a template across all geometries of the dataset and dimensionality reduction to capture principal shape variations (Bruse et al., 2016). Moreover, the SSM is a tool that allows the data augmentation procedure, which means that it is possible to generate new realistic geometries (Ostendorf et al., 2024). The aim of this work is to conduct a population-based morphological and fluid dynamic study to investigate the effects of VA ECMO on flow distribution and blood mixing. Specifically, this study seeks to analyze the impact of aortic morphology on the watershed zone's position and flow characteristics. We leveraged the capability of the SSM to expand our initial dataset with newly synthesized aortic geometries, whose morphology results from a combination of the original shapes. Then, a morphological analysis was performed to identify the most representative geometries within the augmented population. CFD simulations were then conducted on these selected geometries to assess how morphological differences influence hemodynamics. Based on the results of these initial simulations, a subset of geometries with the most significant hemodynamic features was selected for further analysis under ECMO-supported conditions. These additional simulations aimed to determine whether aortic morphology significantly impacts hemodynamics even in the presence of ECMO support. By integrating SSM and CFD, this study provides novel insights into the complex hemodynamics of VA ECMO, contributing to a better understanding of patient-specific factors that influence ECMO outcomes.

2 Materials and methods

The main steps of the procedure followed in this study are outlined in the following section and visually represented in Figure 1. Briefly, starting from an initial dataset of geometries, an augmented dataset of synthetic geometries was generated by developing an SSM. Through morphological inspection, the geometrically most representative geometries were selected for the healthy cases' CFD simulations. Based on the hemodynamic analysis of these results, the most significant geometries were identified for simulations with ECMO support.

2.1 Dataset generation

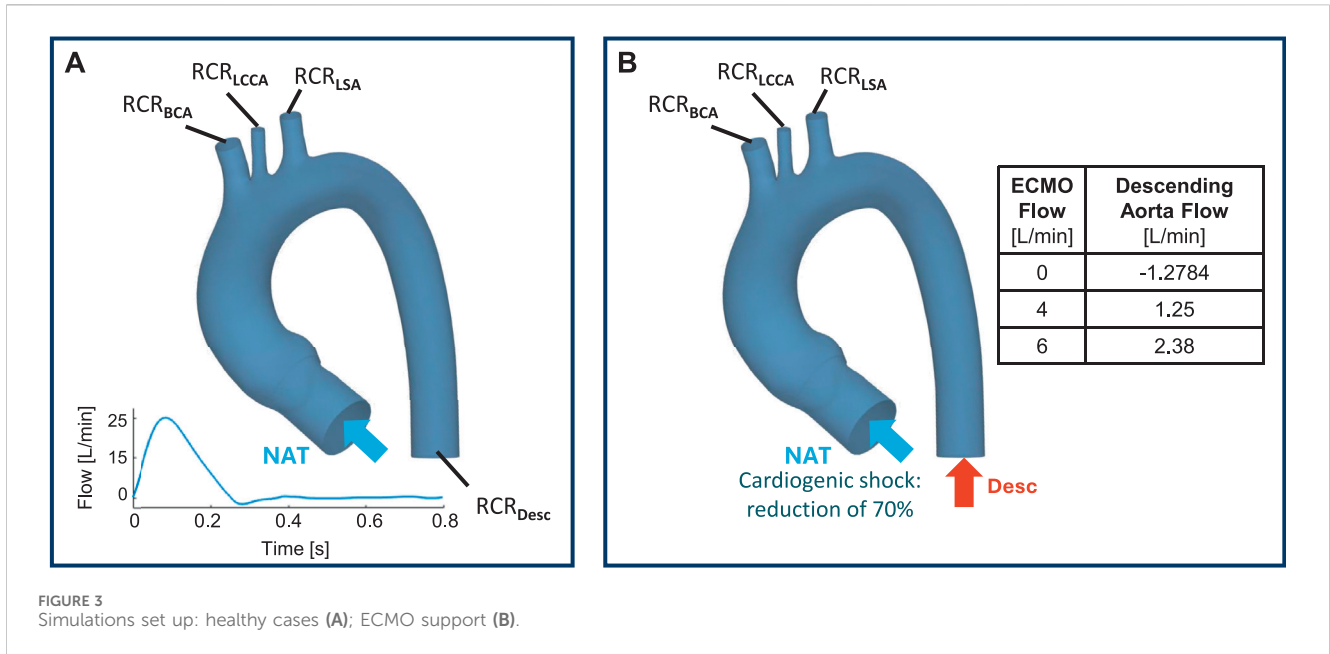
This study considered an initial population consisting of 19 healthy thoracic aortas. The CT scans were performed with a 320-detector scanner (Toshiba Aquilion One, Toshiba, Japan) using



an iodinated contrast medium. The images are characterized by an average pixel size of 0.625 mm and a slice thickness of 0.5 mm . Starting from this population, an SSM was developed. The non-rigid registration of a template on all the other target meshes of the dataset was achieved by using the novel algorithm described in Scarpolini et al. (2023). Given its central role, the template geometry was computed through an iterative procedure. Starting from an initial representative shape, point correspondences were optimized and updated iteratively until convergence was reached, defined as a Euclidean distance change below 0.1 mm . This algorithm enabled the inclusion of supra-aortic vessels in the analysis of the thoracic aorta by employing a multi-scale approach, coupled with the introduction of landmarks at the vessel's open boundaries. Regarding the dimensionality reduction part, Principal Component Analysis (PCA) was applied, which allowed us to go from 19 meshes with 25,000 nodes to 19 meshes with 19 principal components, also called modes m . An augmented dataset of new realistic aortic geometries was generated by varying the standard deviation (SD) of each mode between ± 3 . Since the modes are uncorrelated and ordered by decreasing variance, more geometries were retained for the first modes, using a unit step for the SD, compared to the later ones, for which only the change to $+3\text{ SD}$ was maintained. This choice was driven by the goal of creating an augmented dataset with maximum heterogeneity, and keeping a uniform step size for the last modes did not result in significant geometric changes, as the explained variance is less than 1%.

2.2 Quantitative analysis

A quantitative analysis was conducted to evaluate the morphological differences between the generated shapes and the template. First of all, the centerlines of the vessels with the associated geometric characteristics were extracted through the VMTK software. This operation creates four poly-lines, each connecting the inlet at the aortic root to one of the four outlets: BCA, LCCA, LSA, and descending aorta. The seven characteristic tracts of the thoracic aorta (total aorta, ascending aorta, arch, descending aorta, BCA, LCCA, LSA), represented in Figure 2A, were computed starting from these poly-lines by applying the *branchextractor* operator coupled with an in-house script. The *branchextractor* separates each polyline into different tracts every time the maximum inscribed radius changes, so it was possible to obtain the seven segments working with the Centerline-Id and the Tract-Id. For each of the extracted parts (i) length, (ii) tortuosity: length of a line divided by the distance of its endpoints, (iii) maximum inscribed sphere radius (referred to as "radius" for the sake of brevity), (iv) curvature: inverse of the radius of the local osculating circle, and (v) torsion: the amount by which the osculating plane rotates along the line, were calculated. For points (iii) to (v) mean and standard deviation values were calculated. Finally, the difference of each quantity from the template value was calculated, enabling the selection of 20 geometries for the healthy simulations that accounted for the morphological changes induced by the modes.



Moreover, the mean and standard deviation values were calculated for each quantity over all the centerlines to make a comparison with the template, which represents the average geometry of the population under study.

2.3 CFD simulations

CFD simulations were performed to investigate how different aortic morphologies could impact the oxygenation of supra-aortic branches during extracorporeal membrane oxygenation. Specifically, a set of cases was chosen to simulate healthy conditions based on geometric criteria from the previous quantitative analysis. Following these, a subset of geometries was selected from the healthy cases to simulate ECMO-supported conditions based on differences in terms of mean flows. For all the simulations, the volumetric meshes were generated in ANSA BETA CAE with an automatic in-house script. A polyhedral mesh was adopted, characterized by an average element edge size of 0.5 mm and an imposed target skewness of 0.45. Simulations were performed in *AnsysTM FluentTM* (Ansys, Canonsburg, Pennsylvania, US) resolving the governing Navier-Stokes equations (Equation 1):

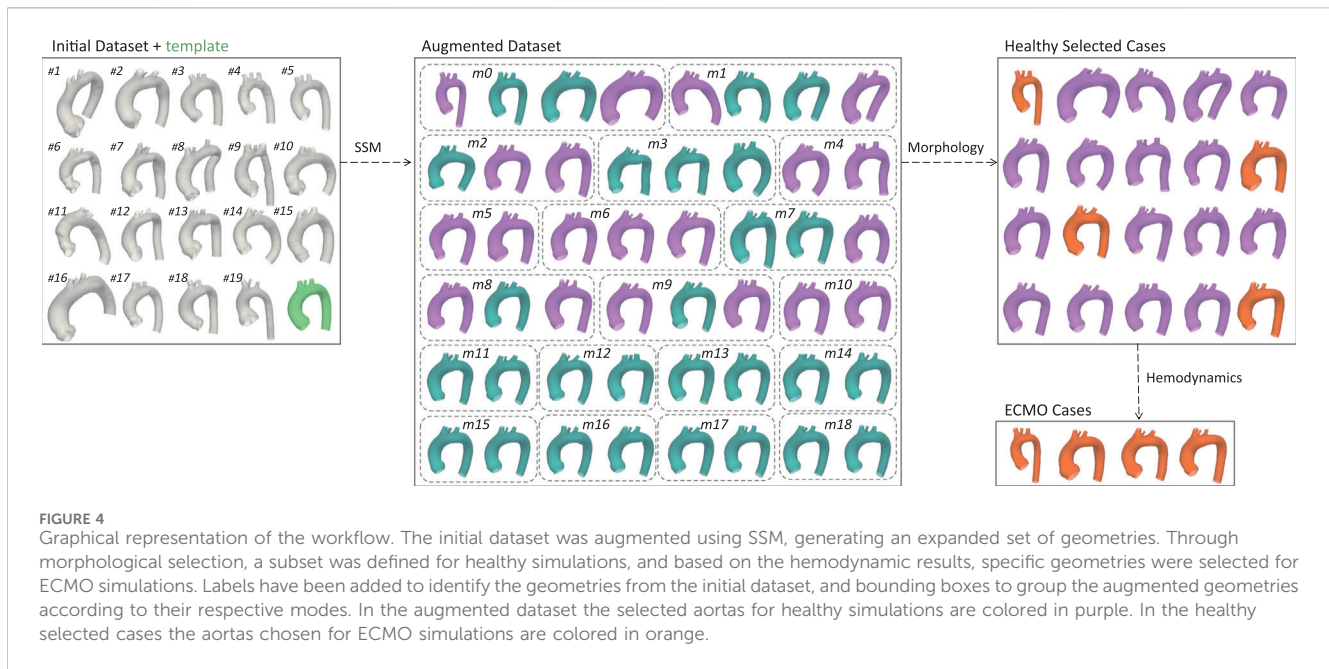
$$\begin{aligned} \nabla \cdot \vec{v} &= 0 \\ \frac{\partial \vec{v}}{\partial t} + (\vec{v} \cdot \nabla) \vec{v} &= -\frac{1}{\rho} \nabla P + \nu \nabla^2 \vec{v} \end{aligned} \quad (1)$$

where \vec{v} is the fluid velocity vector, P is the fluid pressure, ρ the density of blood, and ν the kinematic viscosity of blood. The blood flow was modeled as an incompressible, Newtonian fluid in laminar condition with constant density ρ equal to 1060 kg/m^3 and viscosity ν equal to $3.5 \cdot 10^{-3} \text{ Pa} \cdot \text{s}$. Three cardiac cycles of 0.8 s each were simulated. At the outlet boundaries (BCA, LCCA, LSA, and descending aorta for the

healthy simulations), a pressure condition was applied through a User Defined Function, implementing the three-element Windkessel model (Figure 3A), known as the RCR model. This model consists of a proximal R_p in series with a parallel made of a distal R_d resistance and a capacitance C . The relationships between flow rate $Q(t)$ and pressure $P(t)$ at each branch can be expressed, according to the RCR model, as reported in Equation 2:

$$P(t) = [P(0) - R_p Q(0)] e^{-t/\tau} + R_p Q(t) + \int_0^t \frac{e^{-(t-\bar{t})/\tau}}{C} Q(\bar{t}) d\bar{t} \quad (2)$$

where $\tau = R_d C$ is the time constant that describes the system's response speed to variations in the input function. For each outlet, the parameters were adjusted to maintain a physiological pressure range within the aortic domain and ensure an appropriate physiological flow split. The results were evaluated not only at the outlets but also in three additional sections: pre-arch, post-arch, and descending zone (Figure 2B). The planes for these sections were defined in Ansys Fluent using the 3-points method. The coordinates of these points were obtained through a fully automated process using a Python script that worked with the regions of the centerlines defined in Section 2.2. Based on the Point-Id, the points were identified at: (i) 85% of the ascending aorta for the pre-arch, (ii) 10% of the descending aorta for the post-arch, and (iii) 90% of the descending aorta. The coordinates and the Frenet tangent representing the normal to the point, perpendicular to the centerline, were used to define three planes, on each of which the 3-points are defined. To reduce simulation time, the process was automated using Python scripts and Journal files. The Journal file replicates the GUI command sequence, allowing *AnsysTM FluentTM* to configure input data and run calculations automatically. A single Journal file was used with a for loop to update the mesh path, velocity profile, and coordinate data for



each aorta model. Simulations were run in batch mode via a Python script using the *Subprocess* module, which executed commands in the Windows command prompt while ensuring each simulation finished before starting the next.

2.4 Healthy simulations

For the healthy cases subset simulations, an inlet velocity condition was imposed at the aortic valve level. To investigate the impact of morphology, the same ideal flow rate waveform was used. Velocity values were scaled according to the aortic valve cross-section to impose the same flow (5 L/min) value for all the selected geometries.

2.5 ECMO simulations

For the ECMO subset cases, a Mixture Model was adopted. The Mixture Model solves the momentum, continuity, and energy equations for the phases mixture while introducing the volume fraction for equations of the secondary phases, and algebraic expressions for the relative velocities (Stevens et al., 2017). A two-phase Mixture Model was used to simulate the presence of two fluids, where phase-1 represents the native blood entering from the ascending aorta, while phase-2 is blood from ECMO. Two inlet boundary conditions were set: (i) the pathological cardiac flow from the left ventricle at the aortic valve level and (ii) a constant level of ECMO flow (EF) at the descending aorta (Vignali et al., 2023) (Figure 3B). To simulate the cardiac shock condition, the velocity waveform imposed at the aortic valve level was scaled to obtain a 70 % reduction of cardiac output. Three levels of ECMO support were applied — 0, 4, and 6 L/min—resulting in three simulations for each mesh.

2.6 Evaluation parameters

For each simulated case, results were post-processed in Ansys Fluent, and the following aspects were evaluated: (i) contour plot of total pressure on the aortic wall at systolic peak; (ii) streamlines at systolic peak and contour plot of velocity at the defined planes and (iii) mean flows \bar{Q} at the outlet, defined as reported in Equation 3:

$$\bar{Q} = \int Q_i(t) dt \quad (3)$$

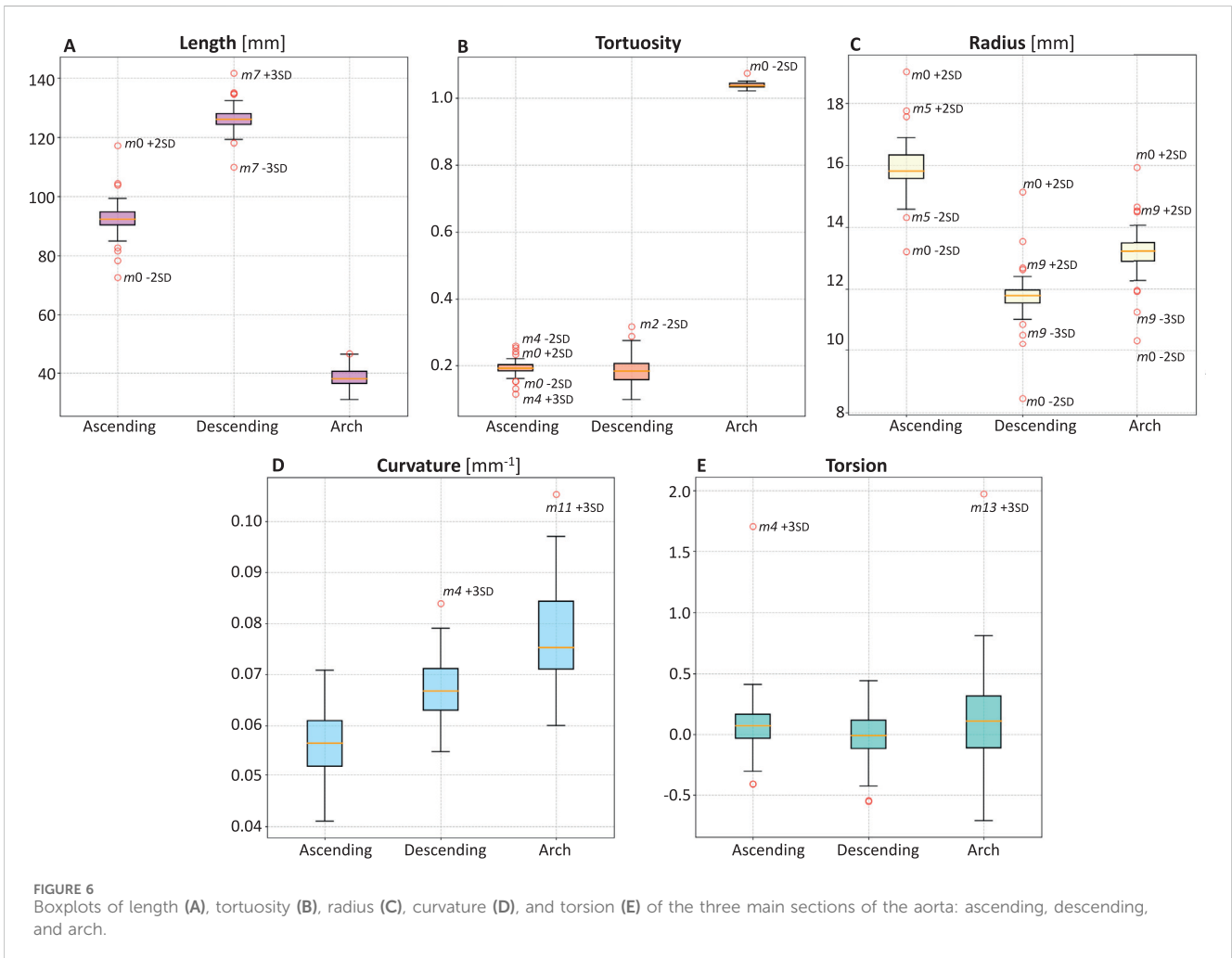
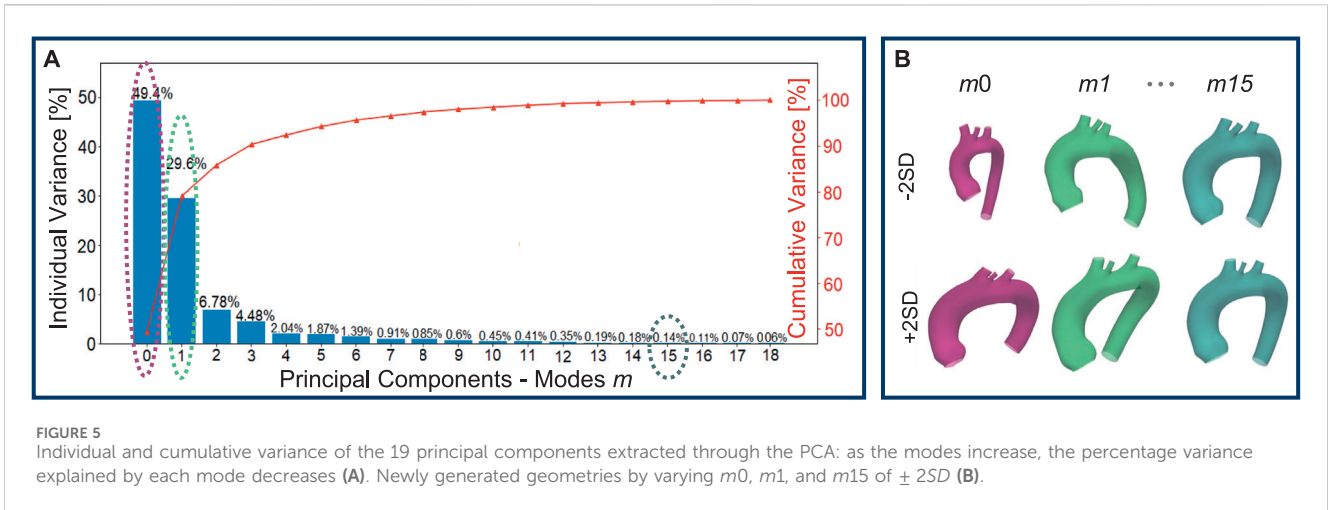
For each CFD simulation, various output parameters were calculated.

3 Results

Figure 4 presents the exploited graphical workflow outlining the methodology employed in this study. By developing an SSM, the initial dataset of 20 geometries was expanded to 48 synthetically generated, anatomically plausible geometries. A morphological analysis was then conducted to identify the 20 most representative geometries, which were subsequently used for CFD simulations under physiological conditions. Based on the hemodynamic analysis of these simulations, the four geometries exhibiting the greatest mean flow deviation from the template were selected for further CFD simulations under ECMO conditions.

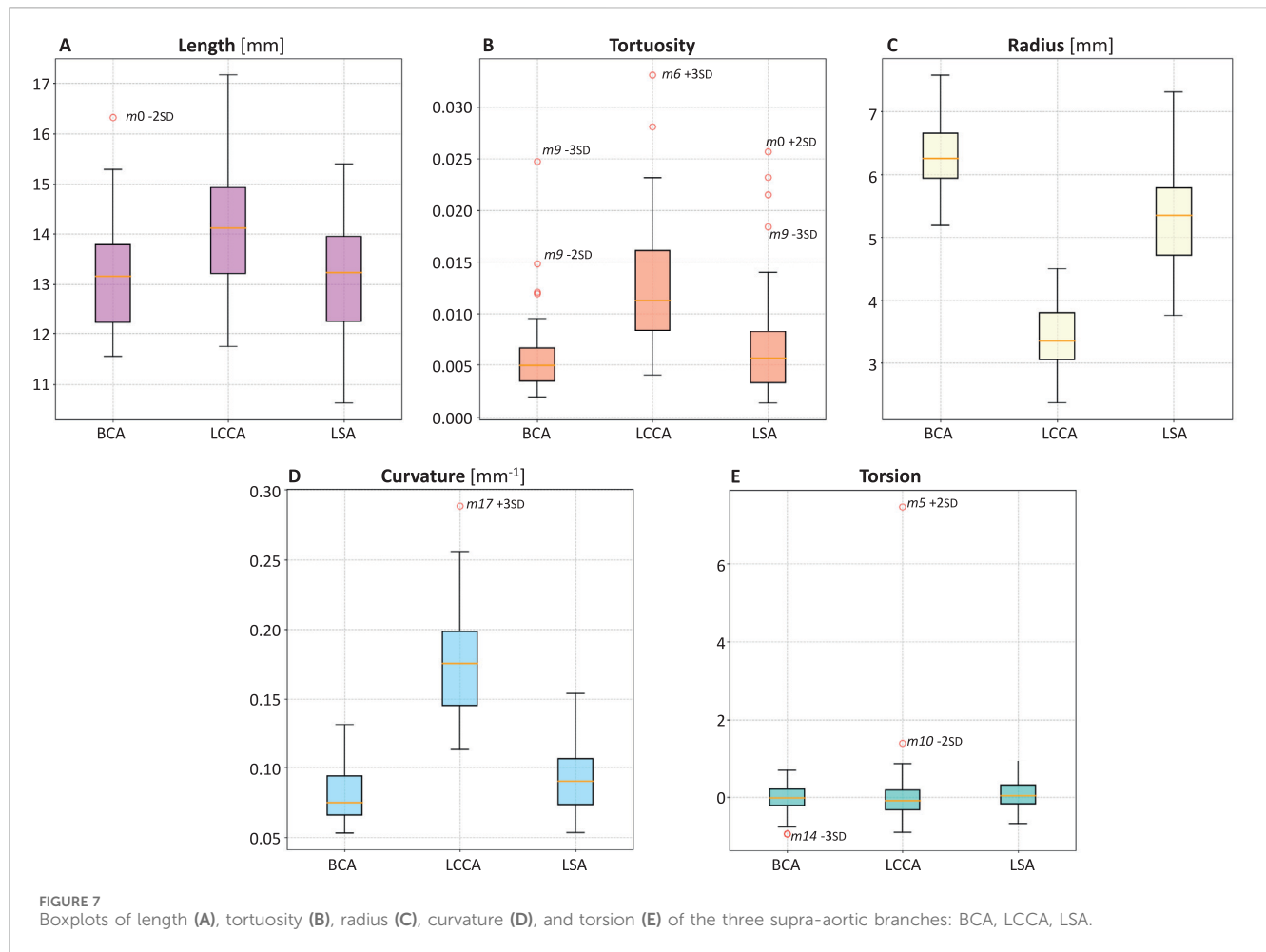
3.1 Dataset generation

A total of 48 geometries (47 novel + template) were generated through the SSM by varying the standard deviation of the PCA modes. A qualitative analysis, conducted through visual inspection of the generated aortic shapes, allows for an understanding of the morphological changes



associated with each principal mode. In particular, Figure 5A, shows that the variance explained by each mode decreases as the mode index increases. As a result, the first modes, which explain the largest portion of the variance, are responsible for global shape variations and predominantly influence global features such as vessel length,

curvature, and radius. Conversely, higher-order modes tend to produce more subtle deformations, especially in the supra-aortic branches, with progressively less noticeable effects on overall shape. For illustrative purposes, Figure 5B, depicts the morphological changes induced by modes m_0 , m_1 , and m_{15} as SD varies from -2 to $+2$.



3.2 Quantitative analysis

Subsequently, a quantitative analysis was conducted on the 47 aortas and the template to define the length, tortuosity, radius, curvature, and torsion of the three main sections of the aorta (ascending, descending, and arch tracts, Figure 6) and of the three supra-aortic branches (BCA, LCCA and LSA, Figure 7). The same features were also defined over the entire aorta to facilitate comparison of the various geometries. Modes 0 to three carry the majority of the variance as regards the length of the ascending, descending, and arch tracts. Extreme cases are visible for $m0$ and $m7$ for the ascending and descending tracts, respectively (Figure 6A). From mode 10 to 18, the total length variation is stable, around 2–3%. The length of each tract was also compared to the corresponding tract of the template, and the lowest variability is in the descending tract.

Concerning tortuosity, most of the variability is observed in the descending aorta, while, in the ascending aorta, there are extreme cases reported by the variations of $m0$ and $m4$ (Figure 6B). From $m10$ to $m18$, there is less and stable variation. The tortuosity of the ascending and descending tracts, compared to the template, shows that the descending tract reaches higher variation.

Mode $m0$ carries most of the radius variance. The ascending tract presents the highest radius values, which decrease in the aortic arch and reach a minimum value in the descending zone (Figure 6C). Apart from $m0$, radius variations compared to the template for each

tract show that the ascending radius has a comparable variation in $m5$ while the arch and descending radius in $m9$.

The curvature values are uniformly distributed between the different geometries, with values ranging from 0.04 to 0.10 mm^{-1} (Figure 6D).

Torsion values are similar between the different geometries, with some extreme cases such as $m4 + 3 \text{ SD}$ for the ascending tract and $m13 + 3 \text{ SD}$ for the arch (Figure 6E).

Table 1 reports the values of the morphological parameters. For each parameter, the values corresponding to the ascending aorta, descending aorta, and aortic arch are shown for the template geometry, along with the minimum and maximum values observed in both the initial dataset (composed of real aortic geometries) and the augmented dataset (synthetically generated shapes).

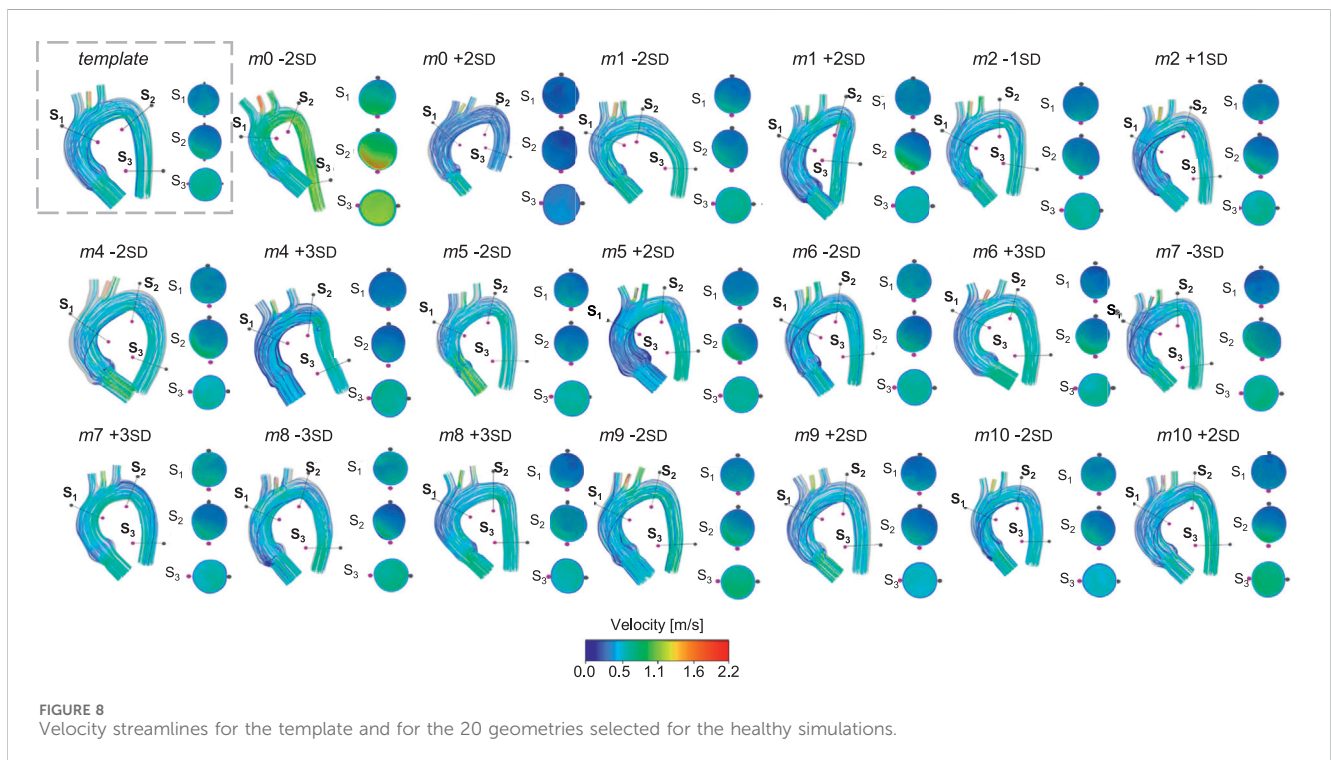
Upon analyzing the differences between the supra-aortic branches, it was found that LCCA has the smallest radius (Figure 7C) and twice the curvature compared to BCA and LSA (Figure 7D).

3.3 Healthy simulations

From the 48 aortas created, 20 geometries were selected from the first 10 modes, as these accounted for 98.5% of the total variability within the dataset. As described above, the principal morphological

TABLE 1 Morphological parameter (Length [mm], Tortuosity, Radius [mm], Curvature [mm^{-1}], and Torsion) values for the template (Temp) and the most extreme geometries in both the initial (Init) and augmented (Aug) datasets. For each parameter, values are reported for the ascending aorta, descending aorta, and arch. The minimum and maximum values are reported with identifying labels in parentheses (#number for real cases and shape mode with SD value for augmented cases).

| Params | Region | Temp | Min-Init | Min-Aug | Max-Init | Max-Aug |
|------------|--------|-------|--------------|--------------------|--------------|--------------------|
| Length | Asc | 89.65 | 55.52 (#5) | 72.61 ($m0 -2$) | 104.37 (#16) | 117.23 ($m0 +2$) |
| | Desc | 124.3 | 112.72 (#13) | 109.85 ($m7 +3$) | 128.23 (#4) | 141.73 ($m7 -3$) |
| | Arch | 38.32 | 28.74 (#7) | 31.28 ($m0 -2$) | 60.15 (#8) | 46.56 ($m1 +2$) |
| Tortuosity | Asc | 0.18 | 0.08 (#5) | 0.12 ($m4 +3$) | 0.25 (#18) | 0.26 ($m8 +3$) |
| | Desc | 0.16 | 0.02 (#9) | 0.1 ($m0 -2$) | 0.39 (#6) | 0.32 ($m2 -2$) |
| | Arch | 1.04 | 1.02 (#2) | 1.02 ($m12-3$) | 1.12 (#5) | 1.07 ($m0 -2$) |
| Radius | Asc | 16.04 | 12.41 (#5) | 13.21 ($m0 -2$) | 21.54 (#16) | 19.03 ($m0 +2$) |
| | Desc | 11.68 | 8.9 (#19) | 8.45 ($m0 -2$) | 16.17 (#16) | 15.14 ($m0 +2$) |
| | Arch | 13.14 | 9.38 (#9) | 10.32 ($m0 -2$) | 17.62 (#16) | 15.92 ($m0 +2$) |
| Curvature | Asc | 0.17 | 0.1 (#16) | 0.04 ($m1 +1$) | 19.06 (#8) | 0.07 ($m14 +3$) |
| | Desc | 0.17 | 0.13 (#1) | 0.05 ($m17 +3$) | 1.8 (#9) | 0.08 ($m4 +3$) |
| | Arch | 0.1 | 0.14 (#10) | 0.06 ($m14-3$) | 5.68 (#11) | 0.11 ($m11 +3$) |
| Torsion | Asc | 4.6 | -4.51 (#1) | -0.41 ($m5 +2$) | 66.93 (#13) | 1.71 ($m4 +3$) |
| | Desc | 0.31 | -1.96 (#8) | -0.56 ($m4 +3$) | 85.5 (#2) | 0.44 ($m10 +2$) |
| | Arch | -0.06 | -32.5 (#11) | -0.71 ($m7 -3$) | 3.09 (#4) | 1.97 ($m13 +3$) |



variations are in: (i) length (approximately 20% for the first modes); (ii) tortuosity (approximately 50%) and (iii) radius (the largest variation is 20% for the total tract of $m0$, followed by 10% for the ascending tract of $m5$ and 10% for the arch radius of $m5$ and

$m9$). The supra-aortic variations were distributed all over the modes, and comparing the three branches, LCCA was half the size compared to BCA and LSA. The 20 selected geometries for the healthy cases are: $m0 \pm 2$ SD, $m1 \pm 2$ SD, $m2 \pm 1$ SD, $m4 -2/+3$ SD,

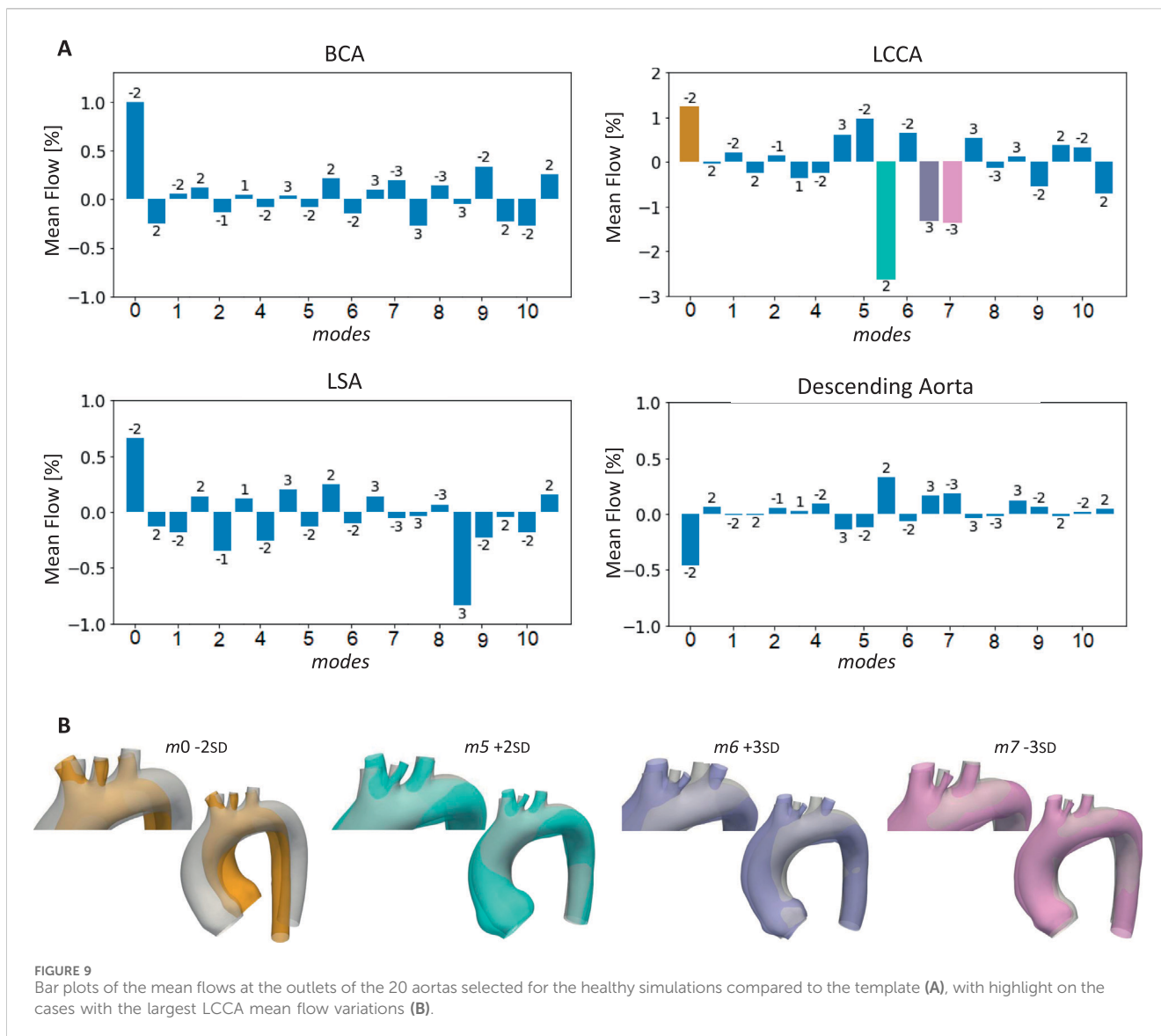


FIGURE 9 Bar plots of the mean flows at the outlets of the 20 aortas selected for the healthy simulations compared to the template (A), with highlight on the cases with the largest LCCA mean flow variations (B).

m5 ± 2 SD, *m6* -2/+3 SD, *m7* ± 3 SD, *m2* ± 3 SD, *m9* ± 2 SD, *m10* ± 2 SD + the template.

Pressure values across the 20 aortic geometries were compared to assess variations related to morphological changes. Overall, pressures remained consistent among all cases, with values ranging around 120–130 mmHg, and showing a physiological decrease from the ascending to the descending aorta. Figure 8 represents the streamlines for the simulated healthy cases. It is worth noting that *m0* -2 SD and *m1* +2 SD velocity reached the highest values. This phenomenon can be motivated by the arch shape and cross-section. In fact, the arch radii of *m0* -2 SD and *m1* +2 SD (10.32 mm and 12.49 mm, respectively) resulted to be lower in comparison with the template (13.14 mm), while the tortuosities (4.63 and 3.29, respectively) appeared to be higher (2.78). This behavior can be associated with the arch shape (gothic arch Margarint et al. (2024); Marrocco-Trischitta et al. (2020)) in general, of these two given cases. Across all supra-aortic branches, LCCA had the highest velocity. This can be motivated by the fact that LCCA exhibited a reduced mean radius (3.4 ± 0.5 mm) in comparison with BCA (6.3 ± 0.47 mm) and LSA (5.3 ± 0.79 mm).

Another morphological feature that influenced the streamlines was the common origin of BCA and LCCA, defined as the Bovine arch type. The geometries exhibiting these variations (*m0* -2 SD and *m1* +2SD) reached higher velocity values compared to the ones with the standard branching pattern. The bar plots in Figure 9 display the percentage of mean flow at the outlets (BCA, LCCA, LSA, and descending aorta) for all the healthy simulated cases with respect to the template mean flow. The largest mean flow variations were found in LCCA, in particular in *m5* +2 SD, followed by *m0* -2 SD, *m6* +3 SD, and *m7* -3 SD. Given this, the four above-cited cases were selected for the subsequent ECMO simulations.

3.4 ECMO simulations

The pressures for the four simulated ECMO cases are reported in Figures 10A,B, for systolic peak and diastolic phase, respectively. In the absence of ECMO support, the simulated cardiogenic shock of 70% caused a significant pressure drop, reaching a minimum value

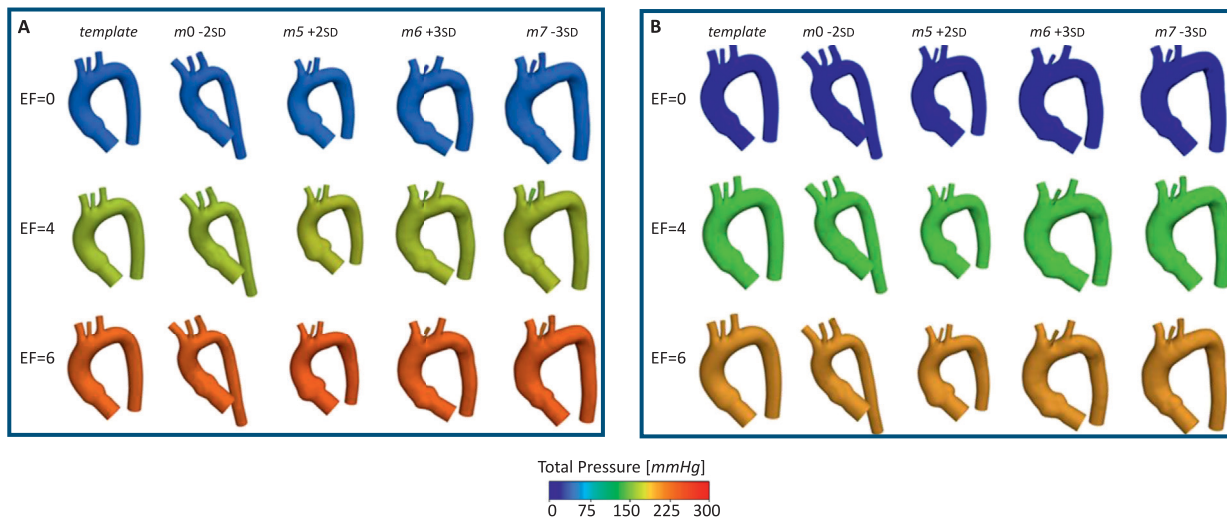


FIGURE 10 Total pressure for the template and the four aortas selected for the ECMO simulations, at different EF levels [L/min], for: systolic peak (A) and diastolic phase (B).

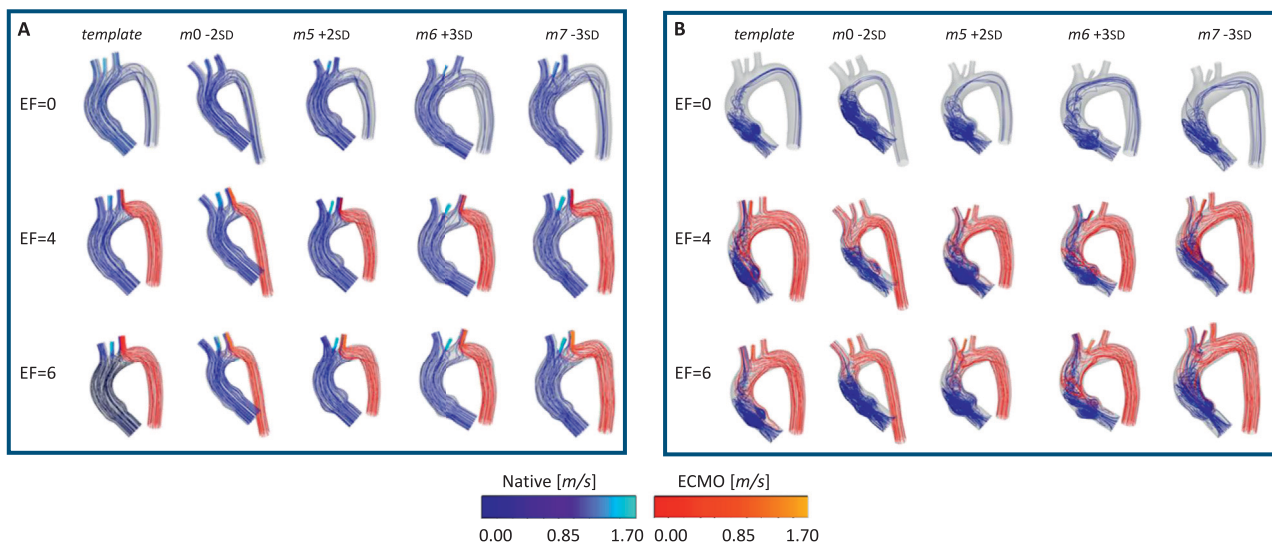


FIGURE 11 Velocity streamlines for the template and the four geometries selected for the ECMO simulations, at different EF levels [L/min], for: systolic (A) and diastolic phase (B).

of approximately 50 mmHg. At 4 L/min ECMO support level, the pressure on the wall of the aorta during systolic peak exceeds the healthy value, reaching 160 mmHg. At a flow rate of 6 L/min, the pressure reaches even higher values, with peaks of 300 mmHg at systole. This behavior of pressure increase as a function of ECMO level is in accordance with the literature and the clinical evidence (Jiang et al., 2024; Gu et al., 2022; Yambe et al., 2024). By comparing the different geometries, the pressure values appear to be similar, and no significant difference in behavior emerged. The velocity streamlines for the four simulated ECMO cases are reported in Figures 11A,B, for the systolic peak and diastolic phase, respectively.

For all cases, it was possible to qualitatively assess the native - ECMO flow mixing zone. Concerning the systolic peak (Figure 11A), at an ECMO level of 4 L/min, the mixing zone is located in the LSA at the systolic peak for all the four considered geometries. The increase of ECMO support level to 6 L/min causes the mixing zone to shift into the aortic arch, between LCCA and LSA. Concerning the diastolic phase (Figure 11B), it is possible to observe that the mixing always goes beyond the BCA level and reaches the ascending aorta both at 4 L/min and 6 L/min. By comparing different geometries, it is observed that the mixing zone position is not affected by morphological variations at the systolic peak, nor at diastole.

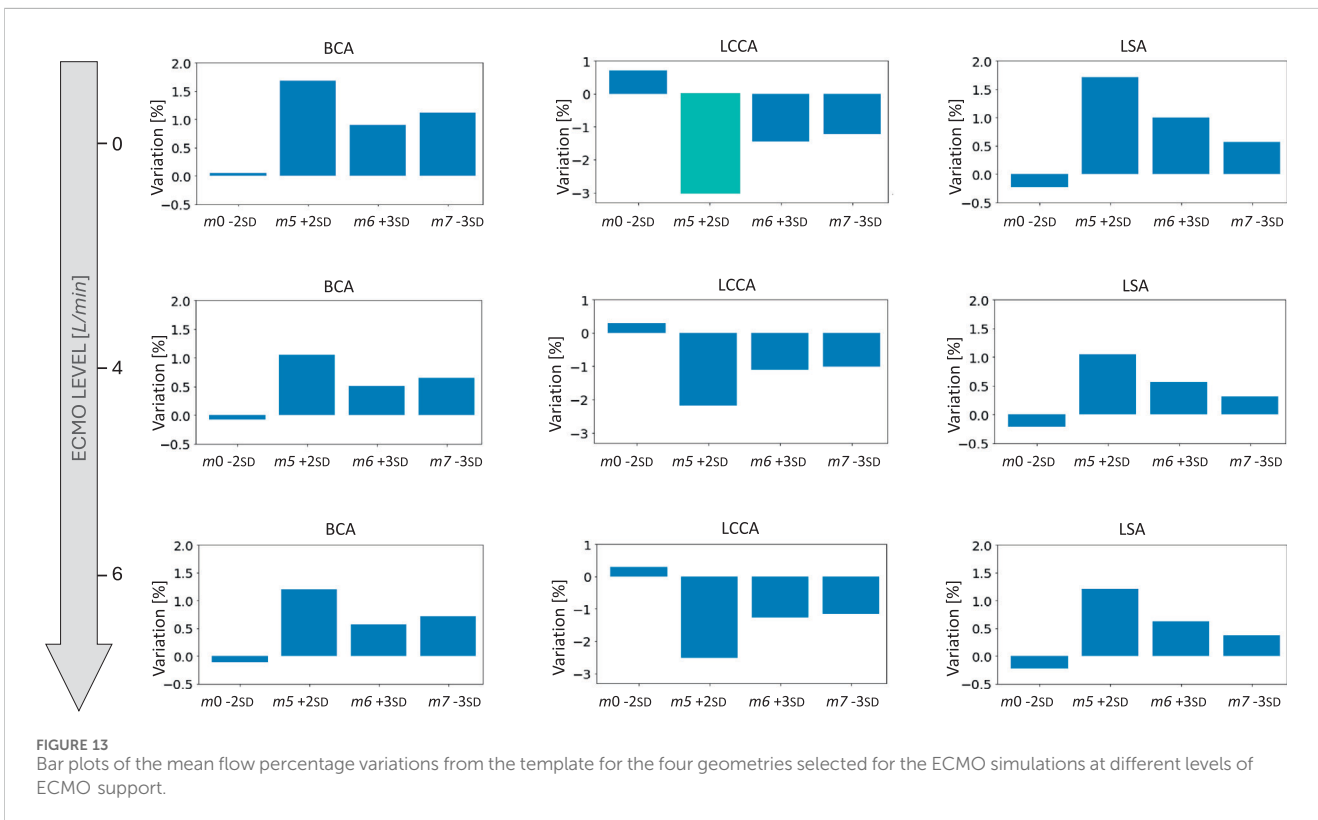
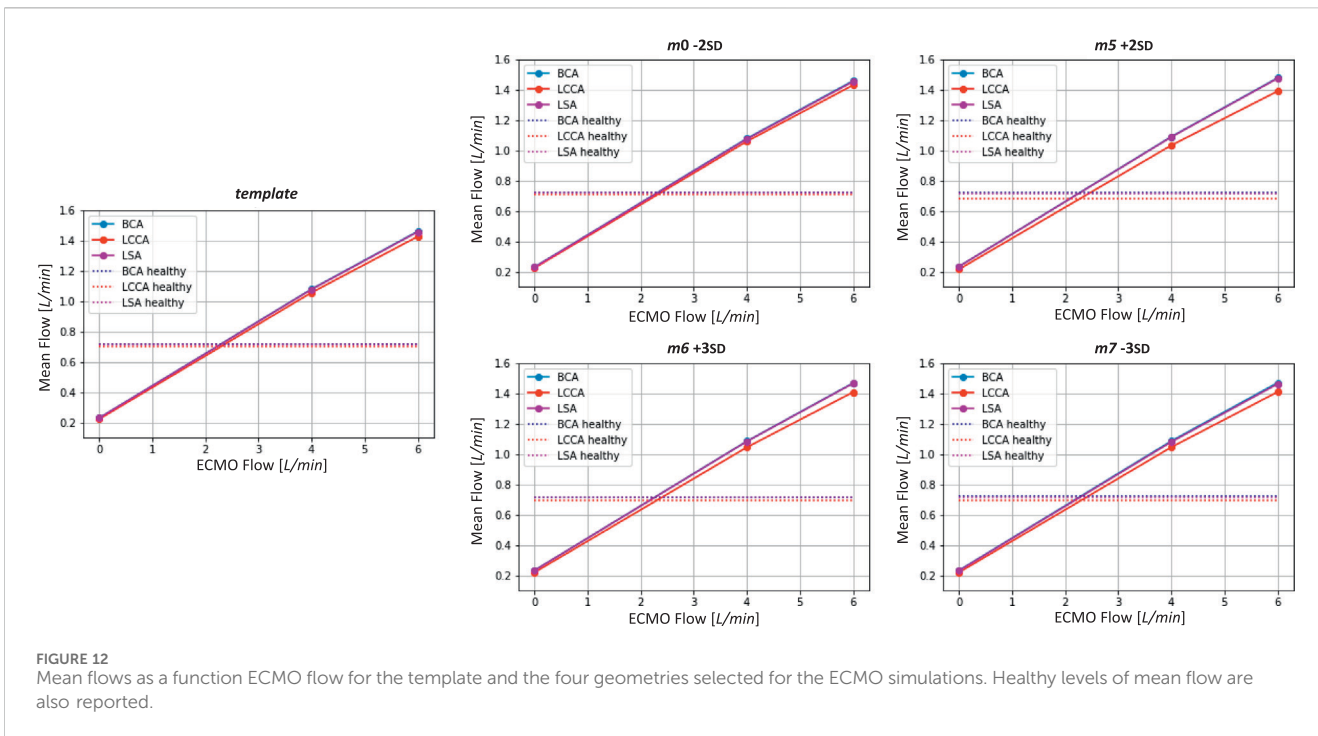


Figure 12 shows the mean flow as a function of ECMO support levels for the three supra-aortic branches, with the healthy levels reported as reference. It is interesting to observe that the healthy level is always reached and the mean flow trend appears to be approximately linear in all the aortas, as already observed in

previous works (Vignali et al., 2023). A quantitative comparison with the template was presented in the bar plots of Figure 13, where the mean flow percentage variations are represented. It is possible to observe that the differences in mean flows are limited, in the range between -3% and $+2\%$. The maximum variation is found in the

LCCA mean flow of $m5 + 2$ SD, in which the flow encountered a reduction of approximately 3% in the condition of absence of ECMO support. This behavior can be explained by the 20% $m5 + 2$ SD radius variation that emerged from the quantitative analysis. As can be seen from Figure 9B, the four geometries presented the Bovine arch type variation in the branching pattern, with the common origin of BCA and LCCA.

4 Discussion and conclusion

This study employed a novel combination of SSM and CFD to investigate the impact of aortic morphology on hemodynamics during VA ECMO support. The SSM approach successfully generated 48 different aortic morphologies, expanding the dataset beyond the initial patient-specific cases (Augmented Dataset of Figure 4). Figure 5 provides valuable insights into the role of principal component modes in capturing morphological variations. Panel A demonstrates that the variance explained by each mode decreases as the mode index increases. The ability of the first few modes to describe major structural changes suggests their potential in characterizing patient-specific aortic morphology for hemodynamic analysis. Additionally, Figure 5B highlights the morphological variations of three modes across a range of standard deviations. The variations of the first modes ($m0$ and $m1$) predominantly affect the global shape, influencing parameters such as aortic arch curvature and vessel diameter. In contrast, latter modes, specifically $m15$ in the example, introduce localized modifications and subtler changes, primarily affecting the supra-aortic vessels. Such local variations may influence secondary flow structures and localized hemodynamic stress distributions, which have been shown to play a role in vascular remodeling and pathology development (Li et al., 2023; Johnston et al., 2021). A quantitative morphology analysis was adopted to select a subset of cases for healthy and ECMO support simulations. The morphological characterization of the dataset revealed key variations in aortic segment properties such as length, tortuosity, radius, curvature, and torsion. Notably, modes 0 and seven exhibited the most extreme variations in length for the ascending and descending aorta, respectively (Figure 6A). Tortuosity varied significantly in the descending aorta (Figure 6B), which may have important implications for flow disturbances and the formation of secondary flow structures. The radius of the aorta showed the highest variation in the ascending portion (Figure 6C), which could affect local velocity profiles and pressure distributions. The results demonstrated that variations in aortic geometry influence the position and characteristics of the watershed zone, thereby affecting oxygenation distribution. These findings align with previous computational studies (Cheng et al., 2014; Khodaei et al., 2022), which have highlighted the role of anatomical variability in ECMO circulatory support. To evaluate the anatomical plausibility of the generated aortic geometries, we compared their morphological parameters with those of the real anatomies in the original dataset. Table 1 includes the minimum and maximum values observed for each parameter in both the initial and augmented datasets. The results show that the synthetic geometries lie within physiologically reasonable bounds, consistent with those found in real subjects. Slight deviations are observed for curvature and torsion, where the maximum values in the initial dataset are significantly higher than those in the augmented one. This is likely due to the lower variance explained by the

higher-order modes used to generate the extreme synthetic shapes, where stronger morphological deviations would require higher SD values than the $\pm 2/\pm 3$ range adopted in this study. This comparison supports the anatomical validity of the augmented dataset and highlights directions for future refinement.

Among the supra-aortic branches, the LCCA exhibited the smallest radius and the highest curvature values (Figures 7C,D), suggesting a more pronounced susceptibility to flow disturbances. The total pressure distribution remained relatively consistent across the 20 healthy simulations, with pressures around 120–130 mmHg in the ascending aorta, gradually decreasing in the descending aorta. This suggests that aortic morphological variations alone do not significantly alter systemic pressures under normal cardiac output conditions. However, localized pressure gradients in more tortuous geometries indicate potential areas of increased flow resistance. Flow streamlines in Figure 8 revealed distinct patterns influenced by arch morphology and branching configuration. In particular, geometries with increased tortuosity values ($m0$ and $m4$) exhibited higher velocity gradients and a more anteriorly positioned watershed zone. The mean flow distribution across supra-aortic branches showed substantial variations, particularly in LCCA (Figure 9A). Geometries featuring a bovine arch (Figure 9B) exhibited the largest deviations from the template, reinforcing the notion that anatomical variations at the arch level can significantly impact cerebral and upper-body perfusion. This corroborates findings from previous numerical studies indicating that complex aortic morphologies at the arch level may exacerbate flow disturbances and contribute to differential hypoxemia (Lo Russo et al., 2024; Syperek, 2020). Additionally, the presence of a bovine arch-type anatomy was associated with altered flow dynamics in supra-aortic branches, further emphasizing the role of anatomical variability in patient-specific ECMO outcomes.

The ECMO simulations demonstrated a marked increase in total pressure with higher ECMO flow rates (Figure 10). At 4 L/min, pressures exceeded physiological levels, reaching 160 mmHg, while at 6 L/min, localized peak pressures approached 300 mmHg. These elevations reinforce concerns regarding increased left ventricular afterload, which may compromise cardiac function and necessitate additional unloading strategies (Schrage et al., 2018; Distelmaier et al., 2020; Kishi, 2020; Jiang et al., 2024; Russo et al., 2019). The watershed zone position was highly dependent on ECMO support levels, as depicted in Figure 11. At 4 L/min, mixing predominantly occurred near the LSA, whereas at 6 L/min, the mixing region shifted into the aortic arch, between LCCA and LSA. During diastole, retrograde ECMO flow extended beyond the BCA, influencing the oxygenation distribution in the ascending aorta. Despite morphological variability, the watershed zone location remained relatively stable across different geometries. Mean flow distributions followed a largely linear trend with increasing ECMO support (Figure 12), suggesting a predictable redistribution pattern. Importantly, in all cases, healthy-level mean flow was restored, confirming ECMO's role in maintaining systemic perfusion. However, cases with significant arch morphological deviations exhibited minor deviations in flow ratios, particularly in LCCA. The percentage variations in mean flow across different ECMO levels remained within -3% to $+2\%$ (Figure 13), with the most significant change observed in LCCA for $m5 + 2$ SD. This reduction in LCCA flow may be linked to local geometric constraints, emphasizing the need for individualized ECMO planning, particularly in cases with altered arch anatomy (Ahmed et al., 2022).

These findings are consistent with prior research (Nezami et al., 2021), which suggests that higher ECMO support levels may contribute to retrograde flow dominance, potentially leading to compromised oxygen delivery to cerebral and upper-body perfusion. The primary limitation of this study is the exclusion of the entire aortic morphology, as the model did not incorporate the abdominal aorta and iliac regions. This omission may influence the overall pressure and flow redistribution dynamics, particularly under ECMO support. Additionally, patient-specific boundary conditions were not included, which may limit the direct clinical applicability of the results. Moreover, although the computational model captures major hemodynamic trends, it inherently relies on assumptions and simplifications. Another important aspect, not included in the current scope of this study, is the characterization of helical flow structures. Helical flow in the aorta has been shown to play a protective physiological role by promoting smooth blood transport, stabilizing flow patterns, and reducing the formation of disturbed shear regions (Morbiducci et al., 2011; Gallo et al., 2012). Alterations in flow helicity have also been observed in pathological conditions, such as in patients with bicuspid aortic valves and aortic dilation, where the disruption of normal helical patterns may have clinical implications (Garcia et al., 2017). Quantifying helicity-related metrics in future simulations could thus enhance the understanding of flow dynamics under ECMO support and serve as a robust quantitative tool for assessing the mixing interface between native cardiac output and the ECMO jet. Additionally, it could be significant to evaluate the effect of the wall movement on the aortic hemodynamics (Capellini et al., 2018; 2021; Calò et al., 2023). Future studies should focus on expanding the dataset to include pathological aortic geometries, such as those encountered in atherosclerosis or aortic dissection, to further elucidate the role of vascular remodeling in ECMO hemodynamics.

An additional relevant aspect that could be explored in future work is whether the hemodynamic results obtained from the augmented dataset are consistent with those derived from the original patient-specific geometries. Such a comparison could serve as an additional validation of the fluid dynamic fidelity of the SSM-generated shapes. Nevertheless, it is worth noting that the augmented dataset was generated to preserve anatomical likeliness and geometric realism, as supported by the quantitative morphological analysis presented in this study. Additionally, incorporating validation through *in-vivo* measurements and experimental setups is fundamental to reinforce the credibility of numerical predictions. As recently demonstrated by (Gasparotti et al., 2025), who validated their CFD models using a detailed mock circulatory loop (Vignali et al., 2022; Bardi et al., 2022) combined with phantom-based flow measurements, the inclusion of experimental data provides an additional layer of verification. This dual numerical-experimental approach enhances the robustness of CFD simulations, enabling a more accurate characterization of flow patterns, critical mixing zones, and physiological responses under ECMO support. Future integration of such validation strategies will be essential to strengthen the reliability of computational frameworks and promote their adoption as effective clinical decision-support tools. Overall, this study highlights the critical role of aortic morphology in influencing ECMO hemodynamics. It provides valuable insights into the interplay between aortic morphology and ECMO hemodynamics, reinforcing the need for personalized ECMO strategies to optimize oxygenation and mitigate complications.

Data availability statement

The data that support the findings of this study are available on reasonable request from the corresponding author.

Ethics statement

All procedures performed in studies involving human participants were in accordance with the ethical gold standards of the institutional and regional research committee and with the 1964 Helsinki Declaration and its later amendments or comparable ethical standards. The study was approved by the Committee of the Tuscany Region on 6th of June 2024 (MAGIC, Marcatori di imAGing, fluIdodinamici e moleColari associati o predittivi ad anomalie delle valvole cardiache e della parete aortica, No. 95/2024).

Author contributions

MM: Writing - original draft, Writing - review and editing, Conceptualization. EG: Writing - original draft, Writing - review and editing, Conceptualization, Resources, Supervision. EV: Writing - original draft, Writing - review and editing, Conceptualization, Resources, Supervision. DH: Writing - review and editing, Conceptualization, Resources, Supervision. SC: Writing - review and editing, Conceptualization, Resources, Supervision.

Funding

The author(s) declare that no financial support was received for the research and/or publication of this article.

Conflict of interest

The authors declare that the research was conducted in the absence of any commercial or financial relationships that could be construed as a potential conflict of interest.

Generative AI statement

The author(s) declare that no Generative AI was used in the creation of this manuscript.

Publisher's note

All claims expressed in this article are solely those of the authors and do not necessarily represent those of their affiliated organizations, or those of the publisher, the editors and the reviewers. Any product that may be evaluated in this article, or claim that may be made by its manufacturer, is not guaranteed or endorsed by the publisher.

References

- Ahmed, Y., Lynch, S. R., Haft, J. W., Moll, F. L., van Herwaarden, J. A., Burris, N. S., et al. (2022). Patient-specific computational modeling of different cannulation strategies for extracorporeal membrane oxygenation. *ASAIO J.* 68, e179–e187. doi:10.1097/mat.0000000000001819
- Aljassam, Y., Sophocleous, F., Bruse, J. L., Schot, V., Caputo, M., and Biglino, G. (2024). Machine learning and statistical shape modelling methodologies to assess vascular morphology before and after aortic valve replacement. *J. Clin. Med.* 13, 4577. doi:10.3390/jcm13154577
- Banfi, C., Pozzi, M., Brunner, M.-E., Rigamonti, F., Murith, N., Mugnai, D., et al. (2016). Veno-arterial extracorporeal membrane oxygenation: an overview of different cannulation techniques. *J. Thorac. Dis.* 8, E875–E885. doi:10.21037/jtd.2016.09.25
- Bardi, F., Gasparotti, E., Vignali, E., Avril, S., and Celi, S. (2022). A hybrid mock circulatory loop for fluid dynamic characterization of 3d anatomical phantoms. *IEEE Trans. Biomed. Eng.* 70, 1651–1661. doi:10.1109/tbme.2022.3224581
- Basir, M. B., Lemor, A., Gorgis, S., Patel, K. C., Kolski, B. C., Bharadwaj, A. S., et al. (2023). Early utilization of mechanical circulatory support in acute myocardial infarction complicated by cardiogenic shock: the national cardiogenic shock initiative. *J. Am. Heart Assoc.* 12, e031401. doi:10.1161/jaha.123.031401
- Bruse, J. L., McLeod, K., Biglino, G., Ntsinjana, H. N., Capelli, C., Hsia, T.-Y., et al. (2016). A statistical shape modelling framework to extract 3d shape biomarkers from medical imaging data: assessing arch morphology of repaired coarctation of the aorta. *BMC Med. Imaging* 16, 40–19. doi:10.1186/s12880-016-0142-z
- Calò, K., Capellini, K., De Nisco, G., Mazzi, V., Gasparotti, E., Gallo, D., et al. (2023). Impact of wall displacements on the large-scale flow coherence in ascending aorta. *J. Biomechanics* 154, 111620. doi:10.1016/j.jbiomech.2023.111620
- Capellini, K., Gasparotti, E., Cella, U., Costa, E., Fanni, B. M., Groth, C., et al. (2021). A novel formulation for the study of the ascending aortic fluid dynamics with *in vivo* data. *Med. Eng. and Phys.* 91, 68–78. doi:10.1016/j.medengphy.2020.09.005
- Capellini, K., Vignali, E., Costa, E., Gasparotti, E., Biancolini, M. E., Landini, L., et al. (2018). Computational fluid dynamic study for aorta hemodynamics: an integrated image-based and radial basis functions mesh morphing approach. *J. biomechanical Eng.* 140, 111007. doi:10.1115/1.4040940
- Cheng, R., Hachamovitch, R., Kittleson, M., Patel, J., Arabia, F., Moriguchi, J., et al. (2014). Complications of extracorporeal membrane oxygenation for treatment of cardiogenic shock and cardiac arrest: a meta-analysis of 1,866 adult patients. *Ann. Thorac. Surg.* 97, 610–616. doi:10.1016/j.athoracsur.2013.09.008
- Cosentino, F., Raffa, G. M., Gentile, G., Agnese, V., Bellavia, D., Pilato, M., et al. (2020). Statistical shape analysis of ascending thoracic aortic aneurysm: correlation between shape and biomechanical descriptors. *J. personalized Med.* 10, 28. doi:10.3390/jpm10020028
- Cui, W., Wang, T., Xu, Z., Liu, J., Simakov, S., and Liang, F. (2023). A numerical study of the hemodynamic behavior and gas transport in cardiovascular systems with severe cardiac or cardiopulmonary failure supported by venoarterial extracorporeal membrane oxygenation. *Front. Bioeng. Biotechnol.* 11, 1177325. doi:10.3389/fbioe.2023.1177325
- Distelmaier, K., Wiedemann, D., Lampichler, K., Toth, D., Galli, L., Haberl, T., et al. (2020). Interdependence of va-ecmo output, pulmonary congestion and outcome after cardiac surgery. *Eur. J. Intern. Med.* 81, 67–70. doi:10.1016/j.ejim.2020.07.014
- Du, G., Zhang, J., Liu, J., and Fan, L. (2022). Case report: two cases of watershed phenomenon in mechanical circulatory support devices: computed tomography angiography imaging and literature review. *Front. Cardiovasc. Med.* 9, 893355. doi:10.3389/fcvm.2022.893355
- Gallo, D., Steinman, D. A., Bijari, P. B., and Morbiducci, U. (2012). Helical flow in carotid bifurcation as surrogate marker of exposure to disturbed shear. *J. biomechanics* 45, 2398–2404. doi:10.1016/j.jbiomech.2012.07.007
- Garcia, J., Barker, A. J., Collins, J. D., Carr, J. C., and Markl, M. (2017). Volumetric quantification of absolute local normalized helicity in patients with bicuspid aortic valve and aortic dilatation. *Magnetic Reson. Med.* 78, 689–701. doi:10.1002/mrm.26387
- Gasparotti, E., Vignali, E., Scolaro, M., Haxhiademi, D., and Celi, S. (2025). A computational and experimental study of veno-arterial extracorporeal membrane oxygenation in cardiogenic shock: defining the trade-off between perfusion and afterload. *Biomechanics Model. Mechanobiol.* 24, 1043–1056. doi:10.1007/s10237-025-01952-9
- Gramigna, V., Palumbo, A., and Fragomeni, G. (2024). The influence of different ecmo cannulation site and blood perfusion conditions on the aortic hemodynamics: a computational fluid dynamic model. *Fluids* 9, 269. doi:10.3390/fluids9110269
- Gu, K., Gao, S., Zhang, Z., Ji, B., and Chang, Y. (2022). Hemodynamic effect of pulsatile on blood flow distribution with va-ecmo: a numerical study. *Bioengineering* 9, 487. doi:10.3390/bioengineering9100487
- Jiang, J., Jain, P., Adji, A., Stevens, M., Vazquez, G. M., Barua, S., et al. (2024). Afterload pressure and left ventricular contractility synergistically affect left atrial pressure during veno-arterial ecmo. *JHLT Open* 3, 100044. doi:10.1016/j.jhlt.2023.100044
- Johnston, L., Allen, R., Hall Barrientos, P., Mason, A., and Kazakidi, A. (2021). Hemodynamic abnormalities in the aorta of Turner syndrome girls. *Front. Cardiovasc. Med.* 8, 670841. doi:10.3389/fcvm.2021.670841
- Khamooshi, M., Wickramarachchi, A., Byrne, T., Seman, M., Fletcher, D. F., Burrell, A., et al. (2024). Blood flow and emboli transport patterns during venoarterial extracorporeal membrane oxygenation: a computational fluid dynamics study. *Comput. Biol. Med.* 172, 108263. doi:10.1016/j.combiomed.2024.108263
- Khodae, F., Nezami, F. R., Zampell, B. A., Galper, E., Edelman, E. R., and Keller, S. P. (2022). Effect of anatomical variation on extracorporeal membrane oxygenation circulatory support: a computational study. *Comput. Biol. Med.* 141, 105178. doi:10.1016/j.combiomed.2021.105178
- Kishi, T. (2020). Clinical implication of left ventricular preload and afterload reduction during venoarterial extracorporeal membrane oxygenation. *Int. J. Cardiol.* 320, 124–125. doi:10.1016/j.ijcard.2020.06.013
- Li, F., Zhu, Y., Song, H., Zhang, H., Chen, L., and Guo, W. (2023). Analysis of postoperative remodeling characteristics after modular inner branched stent-graft treatment of aortic arch pathologies using computational fluid dynamics. *Bioengineering* 10, 164. doi:10.3390/bioengineering10020164
- Lo Russo, G. V., Alarouri, H. S., Al-Abcha, A., Vogl, B., Mahayni, A., Sularz, A., et al. (2024). Association of bovine arch anatomy with incident stroke after transcatheter aortic valve replacement. *J. Am. Heart Assoc.* 13, e032963. doi:10.1161/jaha.123.032963
- Malinowski, D., Fournier, Y., Horbach, A., Erick, M., Magliani, M., Kalverkamp, S., et al. (2023). Computational fluid dynamics analysis of endoluminal aortic perfusion. *Perfusion* 38, 1222–1229. doi:10.1177/02676591221099809
- Margarit, I.-M., Youssef, T., Robu, M., Rotaru, I., Popescu, A., Untaru, O., et al. (2024). The management of aortic coarctation associated with hypoplastic arches and particular arch anatomies: a literature review. *J. Personalized Med.* 14, 732. doi:10.3390/jpm14070732
- Marrocco-Trischitta, M. M., Alaidroos, M., Romarowski, R. M., Secchi, F., Righini, P., Glauber, M., et al. (2020). Geometric pattern of proximal landing zones for thoracic endovascular aortic repair in the bovine arch variant. *Eur. J. Vasc. Endovascular Surg.* 59, 808–816. doi:10.1016/j.ejvs.2019.11.019
- Morbiducci, U., Ponzini, R., Rizzo, G., Cadioli, M., Esposito, A., Montevecchi, F. M., et al. (2011). Mechanistic insight into the physiological relevance of helical blood flow in the human aorta: an *in vivo* study. *Biomechanics Model. Mechanobiol.* 10, 339–355. doi:10.1007/s10237-010-0238-2
- Napp, L. C., Kühn, C., Hoepfer, M. M., Vogel-Claussen, J., Haverich, A., Schäfer, A., et al. (2016). Cannulation strategies for percutaneous extracorporeal membrane oxygenation in adults. *Clin. Res. Cardiol.* 105, 283–296. doi:10.1007/s00392-015-0941-1
- Nezami, F. R., Khodae, F., Edelman, E. R., and Keller, S. P. (2021). A computational fluid dynamics study of the extracorporeal membrane oxygenation-failing heart circulation. *ASAIO J.* 67, 276–283. doi:10.1097/mat.0000000000001221
- Ostendorf, K., Bäuml, K., Mastrodicasa, D., Fleischmann, D., Preim, B., and Mistelbauer, G. (2024). Synthetic surface mesh generation of aortic dissections using statistical shape modeling. *Comput. and Graph.* 124, 104070. doi:10.1016/j.cag.2024.104070
- Parker, L. P., Fiusco, F., Rorro, F., Svensson Marcial, A., Brismar, T. B., Broman, L. M., et al. (2024). Venovenous extracorporeal membrane oxygenation drainage cannula performance: from generalized to patient-averaged vessel model. *Phys. Fluids* 36. doi:10.1063/5.0212546
- Pavlushkov, E., Berman, M., and Valchanov, K. (2017). Cannulation techniques for extracorporeal life support. *Ann. Transl. Med.* 5, 70. doi:10.21037/atm.2016.11.47
- Prisco, A. R., Aguado-Sierra, J., Butakoff, C., Vazquez, M., Houzeaux, G., Eguzkitza, B., et al. (2022). Concomitant respiratory failure can impair myocardial oxygenation in patients with acute cardiogenic shock supported by va-ecmo. *J. Cardiovasc. Transl. Res.* 15, 217–226. doi:10.1007/s12265-021-10110-2
- Rao, P., Khalpey, Z., Smith, R., Burkhoff, D., and Kociol, R. D. (2018). Venoarterial extracorporeal membrane oxygenation for cardiogenic shock and cardiac arrest: cardinal considerations for initiation and management. *Heart Fail.* 11, e004905. doi:10.1161/circheartfailure.118.004905
- Rozencwajg, S., Heinsar, S., Wildi, K., Jung, J.-S., Colombo, S. M., Palmieri, C., et al. (2023). Effect of flow change on brain injury during an experimental model of differential hypoxaemia in cardiogenic shock supported by extracorporeal membrane oxygenation. *Sci. Rep.* 13, 4002. doi:10.1038/s41598-023-30226-6
- Russo, J. J., Aleksova, N., Pitcher, I., Couture, E., Parlow, S., Faraz, M., et al. (2019). Left ventricular unloading during extracorporeal membrane oxygenation in patients with cardiogenic shock. *J. Am. Coll. Cardiol.* 73, 654–662. doi:10.1016/j.jacc.2018.10.085
- Scarpolini, M. A., Mazzoli, M., and Celi, S. (2023). Enabling supra-aortic vessels inclusion in statistical shape models of the aorta: a novel non-rigid registration method. *Front. Physiology* 14, 1211461. doi:10.3389/fphys.2023.1211461

- Schenk, A., Fallon, J., Farrell, M., Halter, R., and Yun, J. (2015). "Murine veno-arterial extracorporeal membrane oxygenation (mva-ecmo): a novel tool to study the molecular biology of mechanical circulatory support," in *AMERICAN journal of transplantation* (NJ USA: WILEY-BLACKWELL), 15.
- Schrage, B., Burkhoff, D., Rübsamen, N., Becher, P. M., Schwarzl, M., Bernhardt, A., et al. (2018). Unloading of the left ventricle during venoarterial extracorporeal membrane oxygenation therapy in cardiogenic shock. *JACC Heart Fail.* 6, 1035–1043. doi:10.1016/j.jchf.2018.09.009
- Shen, J., Tse, J. R., Chan, F., and Fleischmann, D. (2022). Ct angiography of venoarterial extracorporeal membrane oxygenation. *Radiographics* 42, 23–37. doi:10.1148/rg.210079
- Singh, G., Hudson, D., and Shaw, A. (2020). Medical optimization and liberation of adult patients from va-ecmo. *Can. J. Cardiol.* 36, 280–290. doi:10.1016/j.cjca.2019.10.038
- Stevens, M., Callaghan, F., Forrest, P., Bannon, P., and Grieve, S. (2017). Flow mixing during peripheral veno-arterial extra corporeal membrane Oxygenation—A simulation study. *J. biomechanics* 55, 64–70. doi:10.1016/j.jbiomech.2017.02.009
- Syperek, A. (2020). *The "Bovine Aortic Arch" in stroke patients: prevalence, embryological development and hemodynamic implications of a common aortic arch branching variation*. Ph.D. thesis. Aus dem Institut für Diagnostische Radiologie und Neuroradiologie der Medizinischen Fakultät der Universität Greifswald
- Tsiouris, A., Protos, A. N., Saikus, C. E., and Jeyakumar, A. K. C. (2023). Fundamentals of weaning veno-arterial and veno-venous extracorporeal membrane oxygenation. *Indian J. Thorac. Cardiovasc. Surg.* 39, 123–133. doi:10.1007/s12055-023-01474-y
- Vignali, E., Gasparotti, E., Haxhiademi, D., and Celi, S. (2023). Fluid dynamic model for extracorporeal membrane oxygenation support and perfusion in cardiogenic shock. *Phys. Fluids* 35488. doi:10.1063/5.0174259
- Vignali, E., Gasparotti, E., Mariotti, A., Haxhiademi, D., Ait-Ali, L., and Celi, S. (2022). High-versatility left ventricle pump and aortic mock circulatory loop development for patient-specific hemodynamic *in vitro* analysis. *ASAIO J.* 68, 1272–1281. doi:10.1097/mat.0000000000001651
- Vrints, C., Andreotti, F., Koskinas, K. C., Rossello, X., Adamo, M., Ainslie, J., et al. (2024). 2024 esc guidelines for the management of chronic coronary syndromes: developed by the task force for the management of chronic coronary syndromes of the european society of cardiology (esc) endorsed by the european association for cardio-thoracic surgery (eacts). *Eur. heart J.*, ehae177. doi:10.1093/eurheartj/ehae177
- Xiong, Z., Yang, P., Li, D., Qiu, Y., Zheng, T., and Hu, J. (2020). A computational fluid dynamics analysis of a patient with acute non-a-non-b aortic dissection after type i hybrid arch repair. *Med. Eng. and Phys.* 77, 43–52. doi:10.1016/j.medengphy.2019.10.019
- Yambe, K., Ishii, T., Yiu, B. Y., Yu, A. C., Endo, T., and Saijo, Y. (2024). Ultrasound vector flow imaging during veno-arterial extracorporeal membrane oxygenation in a thoracic aorta model. *J. Artif. Organs* 27, 230–237. doi:10.1007/s10047-023-01413-z